

Discover high- z BL Lacs by *Swift* and SARA observations with the dropout technique

Y. SHENG,¹ K. IMAM,¹ A. KAUR,² M. AJELLO,¹ A. DOMÍNGUEZ,³ A. RAU,⁴ S. B. CENKO,^{5,6} J. GREINER,⁴ D. H. HARTMANN,^{1,7}
I. COX,¹ S. JOFFRE,¹ A. MCDANIEL,¹ R. SILVER,¹ AND N. TORRES-ALBÀ⁸

¹*Department of Physics and Astronomy, Clemson University, SC 29634-0978, U.S.A.*^a

²*Department of Astronomy and Astrophysics, 525 Davey Lab, Pennsylvania State University, University Park, PA 16802, USA*

³*IPARCOS and Department of EMFTEL, Universidad Complutense de Madrid, E-28040 Madrid, Spain*

⁴*Max-Planck-Institut für extraterrestrische Physik, Giessenbachstraße 1, D-85748 Garching, Germany*

⁵*Astrophysics Science Division, NASA Goddard Space Flight Center, Mail Code 661, Greenbelt, MD 20771, USA*

⁶*Joint Space-Science Institute, University of Maryland, College Park, MD 20742, USA*

⁷*Southeastern Association for Research in Astronomy (SARA), USA*

⁸*Department of Astronomy, University of Virginia, VA 22904, U.S.A.*

Submitted to ApJ

ABSTRACT

The spectroscopic redshift measurement of BL Lac, a class of blazar, is challenging because its spectrum has no or weak emission lines ($\leq 5\text{\AA}$). We estimate the redshift by the photometric dropout technique for a sample of 64 blazars (59 BL Lacs and five blazar candidates of uncertainty type). Two telescopes are utilized to observe the sample: the *Swift* space telescope observes sources in *uvw2*, *uvm2*, *uvw1*, *u*, *b*, *v* filters, while the ground-based telescopes SARA-CT/RM observed sources in *g'*, *r'*, *i'*, *z'* filters. The photometric data are obtained using the *photozpy* package. We fit the photometric data by the LePhare package and report four new high- z ($z > 1.3$) BL Lacs at $2.03^{+0.07}_{-0.05}$, $1.84^{+0.10}_{-0.03}$, $2.04^{+0.16}_{-0.14}$, $2.93^{+0.01}_{-0.04}$ as well as upper limits for 50 sources. The work increased the number of high- z BL Lacs found by this method up to 23. The high- z sources are discussed in the context of the cosmic gamma-ray horizon, blazar sequence, Fermi blazar divide, and masquerading BL Lacs.

Keywords: (galaxies:) BL Lacertae objects: general — galaxies: active

1. INTRODUCTION

As one of the most extreme environments in the universe, active galactic nuclei (AGNs) are characterized by intense gravitational forces, relativistic jets and luminous radiations (Urry & Padovani 1995). These are of great interest for studying particle acceleration mechanisms under unreachable extreme conditions in current laboratories. The supermassive black hole hosted at the center of the galaxy (Fabian 2008) accretes matter from the surrounding accretion disk, which powers the high luminosities of AGNs (Marconi et al. 2004).

The AGNs can be classified based on their orientation toward Earth (Urry & Padovani 1995). Blazars are a type of AGN with the relativistic jet pointing along the line of sight from us, viewed from an angle $\theta_v < 1/\Gamma$ (Blandford & Rees 1978; Marcotulli et al. 2017), where Γ is the bulk Lorentz factor. It emits lights that nearly covers the entire electromagnetic spectrum from low-frequency radio to high-energy gamma rays, with high variability (Perlman 2013). The blazar spectral energy distribution (SED) is characterized by two bumps. One low-energy bump is located from the infrared to the X-ray band, which is caused by the synchrotron radiation of relativistic electrons in the magnetic field. Another bump from the X-ray to gamma-ray band is interpreted as the outcome of inverse-Compton scattering off the synchrotron photons (Maraschi et al. 1994) or the circumnuclear photon field (Dermer & Schlickeiser 1994). The frequency of the synchrotron bump can classify blazars as low synchrotron peaked (LSP) blazars with $\nu_{peak}^S \leq 10^{14}\text{Hz}$, intermediate synchrotron peaked (ISP) blazars with $10^{14} \leq \nu_{peak}^S \leq 10^{15}\text{Hz}$, and high synchrotron peaked (HSP) blazars with $\nu_{peak}^S \geq 10^{15}\text{Hz}$ (Abdo et al. 2010). There is also an additional classification by the

sheng2@clemson.edu

^a A member of the SARA Consortium

emission lines in the optical spectroscopy of blazars (Padovani & Giommi 1995). If blazars show broad emission lines (equivalent width $\geq 5\text{\AA}$) in their optical spectra, they are called Flat spectrum radio quasar (FSRQ). On the other hand, blazars that display no or weak no emission lines (equivalent width $\leq 5\text{\AA}$) are called BL Lacertae (BL Lac) (Maraschi et al. 1994; Ajello et al. 2013). The featureless makes it challenging to measure redshifts from spectroscopy. Nearly 38% of the BL Lacs in the Forth LAT AGN Catalog Data Release 3 (4LAC-DR3) lack redshift measurements (Ajello et al. 2020, 2022).

As an alternative method, photometric redshift measurement has been implemented for sources like gamma-ray bursts (GRBs) (Tagliaferri et al. 2005; Krühler et al. 2011). Photons from blazar interact with the neutral hydrogen along the line of sight, leaving two characteristic dropouts at rest wavelength bluewards of 912\AA (Lyman limit) and 1216\AA ($\text{Ly}\alpha$ forest). The position and the depth of the absorption features are dependent on the distance. Therefore, photometric measurement of the dropouts can be utilized to determine the redshift. Rau et al. (2012) has implemented this technique using simultaneous multi-band photometric data from *Swift*/UVOT (Roming et al. 2005) and Gamma-ray burst Optical/NearInfrared Detector (GROND, Greiner et al. (2007)). The data are fitted to a list of SED templates to obtain the photometric redshift for a sample of 103 blazars from the Second LAT AGN Catalog (2LAC; Ackermann et al. 2011), which yielded six new high- z ($z > 1.3$) BL Lacs. Except for simultaneous observations, the continued Photo- z campaign (Kaur et al. 2017; Kaur et al. 2018; Rajagopal et al. 2020; Sheng et al. 2024) has discovered 13 more new high- z BL Lacs following the same method.

Extragalactic background light (EBL) is the integrated emission from star formation and supermassive black holes, and the reprocessed light due to the interstellar medium over all redshifts (Domínguez & Ajello 2015; Desai et al. 2019), expanding from radio to gamma rays (Franceschini & Rodighiero 2017). Measuring EBL directly is challenging due to the strong foreground and zodiacal light from the Milky Way (Moralejo et al. 2017). Nonetheless, blazars are appropriate objects for measuring EBL indirectly because the attenuation produced by the blazar gamma-ray photons and EBL photons leaves a distinct fingerprint in the blazar SED. The attenuation in the SED can constrain the evolution of the EBL models with redshift (Biteau & Williams 2015; Abdollahi et al. 2018). The higher the redshift, the stronger the attenuation; therefore, looking for high- z sources is essential to probe EBL (Ackermann et al. 2012), motivating the search for high- z BL Lacs. The population study of blazars also calls for more high- z BL Lacs: the unified model, blazar sequence (Fossati et al. 1998), separates FSRQs and BL Lacs based on their spectral properties (Prandini & Ghisellini 2022). However, outliers are found by the photometric high- z BL Lacs from the Photo- z campaign (Sheng et al. 2024), indicating that the spectroscopic redshift surveys might bias the current population model because of the difficulty in the redshift measurement of BL Lac. Therefore, increasing the number of high- z BL Lacs is essential to examine the unified blazar population model.

This paper is a continuation of the Photo- z campaign. Photometric data in ten filters from near-infrared to ultraviolet ($uvw2$, $uvm2$, $uvw1$, u , b , v , g' , r' , i' , z') are obtained from the Neil Gehrels Swift Observatory (Gehrels et al. 2004), 1.0-meter SARA-RM (Southeastern Association for Research in Astronomy at Roque de los Muchachos, La Palma, Spain), and 0.6-meter SARA-CT (Cerro Tololo, Chile) telescopes (Keel et al. 2016). However, the *Swift*/UVOT and SARA data are not always simultaneous due to the availability of the SARA telescopes. A flat cosmological model Λ CDM with $H_0 = 73$ km/s/Mpc, $\Omega_m = 0.3$, $\Omega_\Lambda = 0.7$ is assumed in this work. The paper is organized as: Section 2 introduces the telescopes and observation techniques; Section 3 explains the aperture photometry method; Section 4 illustrates the SED fitting procedures to obtain the photometric redshifts; Section 5 shows the high- z BL Lacs found in this work; Section 6 is the application of high- z BL Lacs; the last Section 7 is a summary of the work presented.

2. OBSERVATIONS

The sample contains 64 blazars from the 3FGL (Acero et al. 2015), 4FGL-DR3 (Abdollahi et al. 2020, 2022), and Third *Fermi*-LAT Catalog of High-Energy Sources (3FHL, Ajello et al. 2017), among which 59 BL Lacs and 5 blazar candidates of uncertain type (BCU) with $E(B-V) \leq 0.3$. The *Swift* observations are obtained via Cycle 18¹ and 19² of Neil Gehrels Swift Observatory Gust Investigator or Targets of opportunities (ToOs). The mode `0x30ed` is requested for the *Swift*/UVOT observation, resulting in a weighted time spent in each filter as $uvw2 : uvm2 : uvw1 : u : b : v = 4 : 3 : 2 : 1 : 1 : 1$. The integrated time across the *Swift*/UVOT filters is ~ 2000 seconds to ensure a good signal-to-noise (SNR).

The photometric data from the optical to NIR band are obtained by the ground observatory SARA-CT/RM. The two observatories are located in Spain and Chile, providing visibility from both hemispheres. The Sloan Digital Sky Survey (SDSS) filters (g' , r' , i' , z') are used for observations. Although the exposures might be split to avoid cosmic-ray and trailing effects, the integrated time over a filter is 15 to 40 minutes to guarantee good SNR. The targets are observed in sets, and each set contains the split exposures in the four SDSS filters. Table 1 presents the target list and the observations dates for our sample.

¹ Proposal number: 1821042; PI: Mr. Sheng

² Proposal number: 1922139; PI: Mr. Sheng

3. DATA ANALYSIS AND CALIBRATIONS

3.1. *Swift* and SARA data analysis

The *Swift*/UVOT and SARA data are analyzed via the Python package *photozpy*. The automatic data analysis pipeline is built for the data reduction and aperture photometry. The package requires HEASoft³ (v.6.31.1 for this paper) and Swift Calibration Database (CALDB)⁴ (v.1.0.2 for this paper) to be installed for the *Swift* data analysis. This is because the *swiftz* module is a wrapper for the UVOTIMSUM, UVOTSOURCE, and *fappend* commands for aligning and combining image extensions and running photometry. The *Swift* data analysis follows the standard pipeline provided by Poole et al. (2008). The source region has a radius of 5'' for all filters to match the calibration from counts to magnitudes. However, the background region has a radius varying from 20'' to 30'', depending on the source density of the field. Instrument response, bad pixel removal, sensitivity and dark corrections are handled by CALDB.

The SARA CCD data was also analyzed using *photozpy*. The data reduction is handled by the *ccdproc* package (Craig et al. 2017). The bias and dark frames remove the electronic and thermal noise. The flat frames correct pixel-to-pixel sensitivity variation of the CCD and the distortions in the optical path. Cosmic rays are moved by *ccdproc* prior to the image alignment by *astroalign* package (Beroiz et al. 2020) to avoid false source detection. Plate solving is completed by *Astrometry.Net* (Hogg et al. 2008; Lang et al. 2010). The *photozpy* also provides source centroiding and FWHM measurement. The FWHM is measured for all the images as the metric for the source and background radius for each night. Figure 1 shows the radius selection for the source and background regions. The *photutils* package (Bradley et al. 2024) performs the aperture photometry, producing instrumental magnitudes. We use standard stars (Smith et al. 2006; Landolt 2009; Albareti et al. 2017) covering both hemispheres to calibrate the instrumental magnitudes. Galactic extinction is applied for both SARA and *Swift*/UVOT magnitudes (Kataoka et al. 2008).

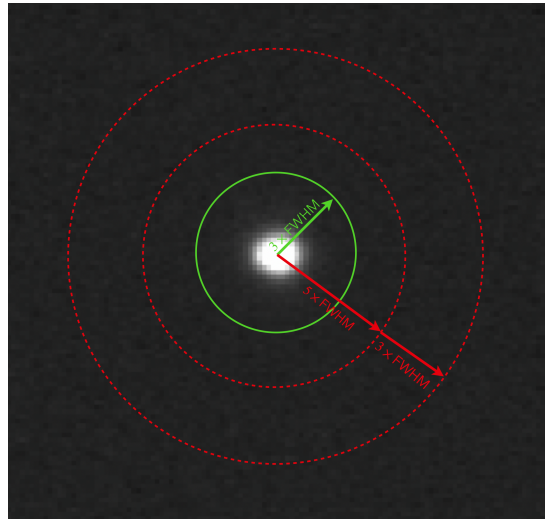


Figure 1. The FWHM is measured in pixel scale. The aperture is centered at the target source with a radius of $3 \times \text{FWHM}$. The background region is an annulus with an inner radius of $5 \times \text{FWHM}$ and an outer radius of $8 \times \text{FWHM}$, which ensures the background regions is ~ 4 times the aperture region.

3.2. Variability correction and cross-calibration

Both *Swift*/UVOT and SARA-CT/RM telescopes observed target sources in sequence in filters. Therefore, we considered variability, usually spanning from minutes to days (Racine 1970; Carini et al. 1991; Urry 1993; Otero-Santos et al. 2022), during the SED fitting. We included an error of 0.1 magnitudes caused by the blazar variability in the systematic uncertainty. This error is based on the measurement in the *uvw2* filter in Rau et al. (2012) and is implemented in the photo-z technique.

Rau et al. (2012) also implemented a cross-calibration between the two instruments under the assumption that the SED of the targets remains the same. Rajagopal et al. (2020) fitted a powerlaw SED with a quadratic function using color terms $g' - r'$ and

³ <https://heasarc.gsfc.nasa.gov/docs/software/heasoft/>

⁴ <https://heasarc.gsfc.nasa.gov/docs/heasarc/caldb/>

$b - g'$ for the cross-calibration formula:

$$b - g' = 0.26(g' - r') + 0.02(g' - r')^2. \quad (1)$$

We calculated the offset in the b filter and applied it to all the *Swift*UVOT filters. Table 2 is a summary of the cross-calibrated photometry.

4. SED FITTING

Lephare v2.2 (Arnouts et al. 1999; Ilbert et al. 2006) is a package for photometric redshift estimation by fitting the photometric data to SED templates with known redshift. It uses χ^2 statistics to check how well the data fits the templates and determines the best-fit SED model. We use three different SED model templates for the sample. The first is a power-law library with 60 templates with power-law indices ranging from 0 to 3 ($F_\lambda \propto \lambda^{-\beta}$, $\beta \in [0, 3]$). The second library is a mix of normal galaxies and AGN/galaxy hybrids intended to fit sources dominated by the host galaxy (Salvato et al. 2008, 2011). The last library is a set of stellar templates to avoid false photometric redshift measurements (Bohlin et al. 1995; Pickles 1998; Chabrier et al. 2000).

Only sources with $E(B - V) \leq 0.3$ will have reliable photometric redshift measurements within $|\Delta z / (1 + z_{\text{sim}})| < 0.15$ for $z > 1.3$, where z_{sim} is the input redshift for the simulation (Rajagopal et al. 2020). To ensure the fitted photometric redshift is within $0.1(1 + z_{\text{phot}})$ of the best-fit value, we only report high- z sources with a probability density of $P_z > 90\%$. We report the redshift upper limits for sources that do not meet the criteria but have $P_z < 90\%$ and $\chi^2 \leq 30$. No redshift is reported for sources with $E(B - V) > 0.3$ since it will produce an unreliable redshift (Rajagopal et al. 2020).

Table 1. *Swift*–UVOT and SARA Observations along with visual extinction values. $A_V = 3.1 \times E(B - V)$

FGL or FHL (Name)	Counterpart (Name)	Class (Type)	RA J2000 ^a (hh:mm:ss)	Dec J2000 ^a (° :':")	<i>Swift</i> Date ^b (UT)	SARA Date ^b (UT)	A_V (mag)
4FGL J0019.6+2022	PKS 0017+200	bll	00:19:37.85	+20:21:45.64	2022 Oct. 17	2022 Oct.16	0.1617
4FGL J0023.9+1603	87GB 002122.5+154553	bll	00:24:01.28	+16:02:33.95	2023 Sep. 20	2023 Sep. 08	0.1758
4FGL J0026.6–4600	1RXS J002636.3–460101	bll	00:26:35.40	–46:01:10.92	2023 Aug. 09	2023 Nov. 19	0.0269
3FHL J0121.8+3808	ILT J012205.88+380445.2 ^d	bll ^d	01:22:06.02 ^d	+38:04:45.41 ^d	2022 Nov. 19	2022 Nov. 06	0.1231
4FGL J0125.3–2548	PKS 0122–260	bll	01:25:18.84	–25:49:04.39	2022 Sep. 10	2022 Sep. 28	0.0401
4FGL J0138.0+2247	GB6 J0138+2248	bll	01:38:01.14	+22:48:08.57	2022 Nov. 20	2022 Nov. 11	0.3212
4FGL J0139.0+2601	WISE J013859.14+260015.7	bll	01:38:59.15	+26:00:15.71	2022 Sep. 20	2022 Oct.16	0.2535
4FGL J0144.6+2705	TXS 0141+268	bll	01:44:33.55	+27:05:03.12	2022 Dec. 06	2022 Nov. 27	0.1899
4FGL J0156.9–5301	1RXS J015658.6–530208	bll	01:56:58.00	–53:01:59.98	2022 Aug. 24	2022 Sep. 28	0.067
4FGL J0237.3+2000	NVSS J023720+200033	bll	02:37:19.77	+20:00:31.76	2022 Sep. 30	2022 Oct.16	0.3625
4FGL J0338.5+1302	RX J0338.4+1302	bll	03:38:29.30	+13:02:15.45	2022 Dec. 31	2022 Nov. 30	0.9293
4FGL J0344.4+3432	1RXS J034424.5+343016	bcu	03:44:24.96	+34:30:18.01	2023 Oct. 15	2023 Oct. 14	0.8228
4FGL J0406.0–5407	SUMSS J040608–540445	bll	04:06:08.66	–54:04:49.89	2023 Nov. 29	2023 Nov. 19	0.0262
4FGL J0439.8–1859	1SXPS J043949.5–190102	bll	04:39:49.73	–19:01:01.42	2023 Jan. 22	2023 Jan. 16	0.1186
4FGL J0500.6–4911	PMN J0500–4912	bll	05:00:38.80	–49:12:16.59	2023 Jan. 16	2023 Jan. 12	0.029
4FGL J0506.9+0323	NVSS J050650+032401	bll	05:06:50.15	+03:23:58.76	2023 Oct. 18	2023 Oct. 14	0.1787
4FGL J0551.0–1622	PMN J0550–1621	bcu	05:50:51.26	–16:21:49.96	2024 Jan. 07	2024 Jan. 03	0.2194
4FGL J0558.8–7459	PKS 0600–749	bll	05:58:46.04	–74:59:05.21	2024 Jan. 01	2023 Dec. 26	0.3405
4FGL J0700.5–6610	PKS 0700–661	bll	07:00:31.25	–66:10:45.23	2024 Feb. 15	2024 Feb. 12	0.3043
4FGL J0746.6–4754	PMN J0746–4755	bll	07:46:42.30	–47:54:55.28	2024 Feb. 21	2024 Feb. 15	0.5356
4FGL J0816.9+2050	SDSS J081649.78+205106.4	bll	08:16:49.78	+20:51:06.44	2021 Mar. 15	2023 Apr. 18	0.1035
3FGL J0851.8+5531	SDSS J085135.93+552834.5	bll	08:51:35.93	+55:28:34.43	2021 Feb. 17	2022 Nov. 30	0.0983
4FGL J0854.3+4408	B3 0850+443	bll	08:54:09.89	+44:08:30.30	2021 Feb. 07	2022 Nov. 27	0.0704

Table 1 continued on next page

Table 1 (continued)

FGL or FHL	Counterpart	Class	RA J2000 ^a	Dec J2000 ^a	Swift Date ^b	SARA Date ^b	A_V
(Name)	(Name)	(Type)	(hh:mm:ss)	(° :′ :″)	(UT)	(UT)	(mag)
4FGL J0859.4+6218	1RXS J085930.5+621737	bll	08:59:30.71	+62:17:30.48	2021 Feb. 05	2022 Nov. 30	0.1657
4FGL J0910.6+3329	Ton 1015	bll	09:10:37.03	+33:29:24.43	2021 Jan. 27	2022 Nov. 27	0.0586
4FGL J0910.6+3329	TXS 0956–244	bll	09:58:20.47	–24:43:59.64	2024 Apr. 14	2024 Apr. 06	0.1409
4FGL J1019.7+6321	GB6 J1019+6319	bll	10:19:50.87	+63:20:01.62	2021 Oct. 27	2022 Nov. 30	0.0221
4FGL J1059.2–1134	PKS B1056–113	bll	10:59:12.42	–11:34:22.78	2023 Feb. 24	2023 Mar. 02	0.073
4FGL J1125.1–2101	PMN J1125–2100	bll	11:25:08.62	–21:01:06.00	2023 Apr. 11	2023 May 23	0.1872
4FGL J1248.3+5820	PG 1246+586	bll	12:48:18.78	+58:20:28.72	2021 Apr. 27	2023 Jun. 09	0.0295
4FGL J1259.8–3749	NVSS J125949–374856	bll	12:59:49.80	–37:48:58.16	2023 Feb. 12	2023 Jul. 07	0.1466
4FGL J1304.9–2107	PKS B1302–208	bcu	13:04:59.07	–21:06:42.46	2024 May. 11	2024 Apr. 06	0.3268
4FGL J1307.6–4259	1RXS J130737.8–425940	bll	13:07:37.98	–42:59:38.99	2023 Feb. 08	2023 Mar. 02	0.2901
4FGL J1427.6–3305	PKS 1424–328	bll	14:27:41.36	–33:05:31.51	2023 Mar. 06	2023 May 23	0.1715
4FGL J1516.8+3651	MG2 J151646+3650	bll	15:16:49.26	+36:50:22.85	2022 Jun. 14	2023 Jun. 09	0.0511
4FGL J1612.4–3100	NVSS J161219–305937	bll	16:12:20.00	–30:59:38.67	2023 Apr. 20	2023 May 23	0.6209
4FGL J1624.6+5651	SBS 1623+569	bll	16:24:32.18	+56:52:27.98	2021 Jun. 28	2023 Apr. 18	0.0235
4FGL J1707.1–1931	PMN J1706–1932	bll	17:06:58.69	–19:31:51.81	2023 Apr. 26	2024 Jul. 17	0.7936
4FGL J1754.2+3212	RX J1754.1+3212	bll	17:54:11.80	+32:12:23.04	2022 Jul. 05	2022 Aug. 08	0.1127
4FGL J1823.5+6858	7C 1823+6856	bll	18:23:32.85	+68:57:52.60	2022 Jul. 28	2022 Oct. 16	0.1759
3FGL J1829.4+5402	1RXS J182925.7+540255	bll	18:29:24.28	+54:02:59.75	2023 Jun. 14	2023 Jun. 09	0.0896
4FGL J1836.4+3137	RX J1836.2+3136	bll	18:36:21.24	+31:36:26.75	2022 Jun. 22	2022 Aug. 08	0.2757
4FGL J1838.8+4802	GB6 J1838+4802	bll	18:38:49.15	+48:02:34.26	2023 Jun. 08	2023 Jun. 09	0.1444
3FGL J1926.8+6154	1RXS J192649.5+615445	bll	19:26:49.89	+61:54:42.34	2023 Jun. 29	2023 Jun. 21	0.1563
4FGL J1946.0–3112	PKS 1942–313	bll	19:45:59.36	–31:11:38.36	2023 May. 29	2023 May 23	0.3454
4FGL J1959.7–4725	1RXS J195945.8–472531	bll	19:59:45.67	–47:25:19.35	2023 Jun. 01	2024 Jul. 17	0.1438
4FGL J2030.9+1935	RX J2030.8+1935	bll	20:30:57.13	+19:36:12.93	2023 Jun. 24	2023 Jun. 18	0.2461
4FGL J2126.1–3922	PMN J2126–3921	bll	21:26:25.20	–39:21:22.27	2022 Aug. 30	2022 Sep. 28	0.091
4FGL J2144.2+3132	MG3 J214415+3132	bll	21:44:15.21	+31:33:39.12	2023 Sep. 21	2023 Oct. 14	0.3884
4FGL J2149.6+0323	PKS B2147+031	bll	21:49:41.87	+03:22:51.43	2023 Aug. 01	2023 Aug. 18	0.2066
4FGL J2243.7–1231	RBS 1888	bll	22:43:40.50	–12:31:01.31	2021 Aug. 08	2023 Jul. 07	0.1421
4FGL J2243.9+2021	RGB J2243+203	bll	22:43:54.74	+20:21:03.78	2023 Aug. 26	2023 Sep. 08	0.1261
4FGL J2325.6+1644	NVSS J232538+164641	bll	23:25:38.12	+16:46:42.71	2021 Jul. 26	2022 Aug. 09	0.0974
4FGL J2352.0+1750	CLASS J2352+1749	bll	23:52:05.84	+17:49:13.75	2023 Sep. 27	2023 Sep. 24	0.118
3FHL J2358.4–1808	NVSS 235836-180718 ^d	bll ^d	23:58:36.78 ^d	–18:07:18.49 ^d	2022 May. 11	2022 Sep. 28	0.068
3FGL J0707.2+6101	TXS 0702+612	bcu	07:07:00.57	+61:10:10.56	2022 Nov. 23	2022 Nov. 27	0.2177
4FGL J0800.9+4401	B3 0757+441	bll	08:01:08.28	+44:01:10.16	2020 Nov. 30	2022 Nov. 27	0.1123
3FGL J0103.4+5336	1RXS J010325.9+533721	bll	01:03:25.96	+53:37:13.30	2020 Jul. 27	2022 Aug. 15	0.9292
3FGL J1138.2+4905	GB6 J1138+4858	bcu ^c	11:38:02.07	+48:58:56.81	2023 Jan. 18	2023 Apr. 18	0.0466
3FGL J1323.9+1405	RX J1323.9+1406	bll	13:23:58.49	+14:06:01.08	2023 Jun. 01	2023 Jun. 21	0.0682
3FGL J1354.5+3705	FIRST J135426.6+370654	bll	13:54:26.69	+37:06:54.58	2023 Jun. 09	2023 Jun. 21	0.0297
3FGL J1500.6+4750	BZB J1500+4751	bll	15:00:48.65	+47:51:15.54	2023 Jun. 20	2023 May 29	0.0722
3FGL J1649.4+5238	87GB 164812.2+524023	bll	16:49:24.99	+52:35:15.00	2023 Jun. 30	2023 Jul. 22	0.1482
3FGL J1702.6+3116	RX J1702.6+3115	bll	17:02:38.80	+31:15:46.66	2023 Jul. 10	2023 Sep. 08	0.0903

^a The optical coordinates are from the 3FGL and 4FGL catalogs, which are used for *Swift*/UVOT and SARA observations.

^b The beginning date of the *Swift* and SARA observations.

^c The source was a BCU when selected. It is classified as a FSRQ in the 4LAC catalog.

^d The coordinates, counterparts and classes are determined by the method implemented in [Joffre et al. \(2022\)](#); [Stroh & Falcone \(2013\)](#); [Paiano et al. \(2017\)](#); [Silver et al. \(2020\)](#); [Kerby et al. \(2021\)](#)

Table 2. *Swift*-UVOT and SARA photometry (AB magnitudes corrected for extinction)

FGL or FHL Name	g'	r'	i'	z'	$uw2$	$uw2$	$uw1$	u	b	v
4FGL J0019.6+2022	20.22±0.12	19.43±0.11	18.99±0.15	19.06±0.46	>22.59	>21.9	>21.81	>21.17	>20.44	>19.62
4FGL J0023.9+1603	20.42±0.21	19.82±0.2	19.24±0.23	>19.27	>22.8	>22.32	>21.98	>21.32	>20.58	>19.77
4FGL J0026.6-4600	18.13±0.08	17.26±0.04	18.38±0.21	17.13±0.18	19.11±0.07	18.87±0.08	18.82±0.07	18.5±0.07	18.38±0.09	18.09±0.13
3FHL J0121.8+3808	17.57±0.06	17.55±0.07	17.13±0.07	17.17±0.14	17.94±0.05	18.03±0.07	17.88±0.07	17.65±0.06	17.57±0.07	17.42±0.12
4FGL J0125.3-2548	19.96±0.19	19.68±0.21	19.45±0.32	17.64±0.2	21.95±0.23	21.46±0.28	21.8±0.36	20.31±0.2	20.03±0.27	>19.51
4FGL J0138.0+2247	18.08±0.07	17.72±0.06	>20.22	17.43±0.13	19.58±0.09	19.62±0.13	19.26±0.11	18.78±0.11	18.18±0.11	18.2±0.2
4FGL J0139.0+2601	17.65±0.02	17.11±0.02	16.84±0.03	16.64±0.05	19.08±0.07	18.99±0.09	18.49±0.08	18.15±0.07	17.79±0.07	17.55±0.1
4FGL J0144.6+2705	19.78±0.09	19.45±0.12	18.78±0.11	18.13±0.19	>21.9	>21.56	>22.01	>21.03	>19.87	>19.16
4FGL J0156.9-5301	17.96±0.03	17.51±0.03	17.33±0.06	16.74±0.11	18.74±0.07	18.76±0.09	18.54±0.06	18.39±0.08	18.08±0.09	17.82±0.14
4FGL J0237.3+2000	18.81±0.08	18.37±0.07	18.24±0.1	18.28±0.26	19.99±0.19	19.84±0.25	19.47±0.21	19.02±0.22	18.93±0.36	>18.22
4FGL J0338.5+1302	17.56±0.08	17.46±0.06	17.34±0.08	17.47±0.21	18.35±0.16	18.73±0.22	18.42±0.22	17.68±0.15	17.58±0.19	17.15±0.22
4FGL J0344.4+3432	18.47±0.09	18.12±0.09	17.61±0.09	16.85±0.12	>19.5	>19.4	>19.2	>19.07	>18.57	17.82±0.31
4FGL J0406.0-5407	18.9±0.11	18.09±0.07	17.73±0.1	18.78±0.84	20.39±0.09	20.19±0.13	19.97±0.11	19.34±0.1	19.12±0.12	18.95±0.21
4FGL J0439.8-1859	17.7±0.04	17.47±0.04	17.41±0.08	16.57±0.12	18.77±0.06	18.84±0.08	18.45±0.08	18.08±0.07	17.76±0.07	17.64±0.11
4FGL J0500.6-4911	18.22±0.04	17.72±0.03	16.92±0.03	17.98±0.3	19.44±0.09	19.23±0.11	18.9±0.1	18.71±0.12	18.35±0.14	17.72±0.17
4FGL J0506.9+0323	19.08±0.08	18.72±0.1	18.64±0.16	>19.05	20.7±0.21	20.5±0.28	20.31±0.27	19.69±0.25	19.18±0.3	18.52±0.33
4FGL J0551.0-1622	>20.5	>20.33	>19.77	>18.44	>22.38	>22.01	>21.58	>21.23	>20.55	>19.79
4FGL J0558.8-7459	19.18±0.97	18.28±0.32	18.48±0.42	18.48±0.86	21.55±0.33	>21.17	20.7±0.26	19.87±0.2	19.44±0.22	19.27±0.36
4FGL J0700.5-6610	16.15±0.01	15.78±0.01	15.51±0.02	15.34±0.04	17.49±0.05	17.51±0.06	17.12±0.06	16.65±0.05	16.25±0.04	16.1±0.06
4FGL J0746.6-4754	16.27±0.03	16.0±0.02	15.83±0.03	15.7±0.07	17.28±0.07	17.2±0.09	16.91±0.08	16.59±0.05	16.35±0.05	16.11±0.08
4FGL J0816.9+2050	18.24±0.03	>21.18	18.83±0.17	>19.46	19.22±0.16	18.88±0.17	18.45±0.11	17.97±0.14	17.65±0.24	16.93±0.25
3FGL J0851.8+5531	18.01±0.02	17.56±0.02	17.22±0.04	17.04±0.1	19.21±0.08	18.98±0.09	18.63±0.09	18.3±0.08	18.14±0.1	17.49±0.12
4FGL J0854.3+4408	16.67±0.01	16.42±0.01	16.27±0.01	16.15±0.03	17.51±0.04	17.37±0.05	17.24±0.05	16.95±0.04	16.73±0.04	16.6±0.07
4FGL J0859.4+6218	19.54±0.07	19.13±0.08	18.94±0.14	18.68±0.33	20.64±0.09	20.43±0.11	20.33±0.11	20.0±0.12	19.65±0.14	19.34±0.22
4FGL J0910.6+3329	16.92±0.01	16.64±0.01	16.47±0.01	16.36±0.03	17.9±0.04	17.77±0.05	17.6±0.05	17.2±0.04	17.0±0.04	16.89±0.06
4FGL J0910.6+3329	20.71±0.7	20.08±0.7	19.5±0.71	>18.44	>22.56	>22.15	>21.59	>21.45	>20.88	>20.15
4FGL J1019.7+6321	17.93±0.02	17.57±0.02	17.46±0.05	17.69±0.21	19.24±0.09	19.25±0.12	19.01±0.12	18.59±0.15	18.03±0.17	17.89±0.31
4FGL J1059.2-1134	17.44±0.06	17.06±0.03	16.66±0.04	16.14±0.07	18.86±0.05	18.69±0.07	18.46±0.06	18.5±0.05	17.54±0.05	17.29±0.07
4FGL J1125.1-2101	18.47±0.07	18.28±0.1	19.15±0.36	>18.57	19.87±0.07	19.65±0.09	19.37±0.08	18.78±0.06	18.52±0.07	18.19±0.1
4FGL J1248.3+5820	15.78±0.0	15.4±0.0	15.16±0.0	14.93±0.01	16.91±0.04	16.73±0.04	16.6±0.04	16.16±0.04	15.88±0.04	15.63±0.04
4FGL J1259.8-3749	>20.18	18.3±0.15	18.99±1.03	>17.9	19.73±0.09	19.56±0.12	19.57±0.13	19.21±0.14	18.6±0.14	17.88±0.16
4FGL J1304.9-2107	20.45±0.72	19.88±0.65	19.45±0.69	>18.49	22.34±0.35	>21.91	>21.57	>21.26	>20.6	>19.9
4FGL J1307.6-4259	16.54±0.01	16.24±0.02	16.05±0.02	15.92±0.06	17.76±0.06	17.69±0.08	17.37±0.06	16.81±0.05	16.62±0.05	16.53±0.08

Table 2 continued on next page

Table 2 (continued)

FGL or FHL Name	g'	r'	i'	z'	$uw2$	$uw2$	$uw1$	u	b	v
4FGL J1427.6-3305	19.22±0.15	17.89±0.07	17.62±0.08	17.02±0.1	21.36±0.13	21.44±0.2	21.04±0.18	20.31±0.15	19.6±0.14	19.17±0.19
4FGL J1516.8+3651	19.95±0.08	19.33±0.08	19.04±0.13	18.96±0.39	>22.62	>22.16	21.69±0.33	20.97±0.31	20.12±0.28	>19.63
4FGL J1612.4-3100	18.25±0.12	17.63±0.09	17.36±0.09	17.59±0.22	19.69±0.25	>18.88	19.57±0.29	18.64±0.18	18.42±0.24	>17.7
4FGL J1624.6+5651	18.48±0.03	17.94±0.04	17.59±0.05	17.96±0.17	19.76±0.09	19.71±0.13	19.32±0.1	18.97±0.1	18.62±0.12	18.47±0.2
4FGL J1707.1-1931	>19.32	18.1±0.2	17.75±0.18	17.77±0.39	>20.93	>20.68	>20.55	>20.27	>19.67	>19.05
4FGL J1754.2+3212	17.39±0.05	17.1±0.05	16.88±0.05	16.66±0.09	18.39±0.06	18.32±0.07	18.13±0.07	17.66±0.06	17.47±0.06	17.31±0.1
4FGL J1823.5+6858	19.41±0.06	18.99±0.07	18.57±0.11	18.7±0.35	>22.36	21.82±0.33	21.4±0.3	20.02±0.16	19.52±0.18	18.9±0.21
3FGL J1829.4+5402	18.28±0.03	18.02±0.04	17.82±0.05	17.62±0.12	19.45±0.08	19.25±0.09	18.94±0.09	18.67±0.08	18.35±0.09	18.08±0.14
4FGL J1836.4+3137	17.95±0.1	17.23±0.06	16.89±0.06	16.93±0.12	19.62±0.12	19.61±0.16	18.98±0.12	18.7±0.12	18.15±0.13	17.56±0.15
4FGL J1838.8+4802	14.79±0.0	14.56±0.0	14.39±0.0	14.26±0.01	15.67±0.04	15.56±0.04	15.41±0.04	15.05±0.04	14.85±0.04	14.75±0.04
3FGL J1926.8+6154	17.31±0.01	17.09±0.01	16.86±0.02	16.8±0.06	18.0±0.05	17.87±0.08	17.78±0.06	17.42±0.05	17.37±0.06	17.24±0.09
4FGL J1946.0-3112	15.97±0.01	15.36±0.01	15.38±0.01	15.32±0.03	17.65±0.18	17.28±0.19	17.19±0.21	16.43±0.17	16.14±0.22	15.26±0.2
4FGL J1959.7-4725	16.47±0.02	16.11±0.02	15.88±0.03	15.69±0.08	17.44±0.05	17.36±0.06	17.16±0.06	16.7±0.04	16.56±0.05	16.5±0.08
4FGL J2030.9+1935	18.15±0.02	17.8±0.03	17.56±0.04	17.6±0.14	18.95±0.08	19.21±0.14	18.96±0.1	18.51±0.1	18.24±0.12	17.71±0.14
4FGL J2126.1-3922	19.98±0.21	19.7±0.24	19.27±0.3	>18.6	>22.36	>21.86	21.38±0.32	20.63±0.31	>20.05	>19.19
4FGL J2144.2+3132	17.57±0.02	17.15±0.03	16.82±0.03	16.44±0.07	21.81±0.36	20.96±0.26	20.5±0.21	19.03±0.1	17.68±0.06	17.26±0.08
4FGL J2149.6+0323	18.1±0.03	17.65±0.03	17.35±0.04	17.07±0.1	19.61±0.12	19.25±0.15	19.0±0.13	18.47±0.12	18.23±0.16	17.94±0.23
4FGL J2243.7-1231	>18.84	>18.62	>18.23	>17.61	19.72±0.09	19.75±0.11	19.57±0.11	19.42±0.14	18.9±0.15	19.12±0.35
4FGL J2243.9+2021	16.05±0.0	15.78±0.01	15.59±0.01	15.44±0.02	17.06±0.04	16.88±0.05	16.71±0.04	16.36±0.04	16.13±0.04	15.92±0.05
4FGL J2325.6+1644	18.69±0.03	18.26±0.03	18.0±0.06	18.09±0.19	19.39±0.11	19.13±0.14	19.19±0.14	19.04±0.18	18.8±0.25	>18.26
4FGL J2352.0+1750	18.05±0.04	17.71±0.04	17.64±0.06	17.82±0.2	19.39±0.09	19.24±0.13	18.93±0.11	18.47±0.1	18.15±0.13	17.71±0.18
3FHL J2358.4-1808	17.87±0.03	17.6±0.03	17.43±0.05	17.0±0.11	19.15±0.07	19.11±0.1	...	18.41±0.09	17.94±0.1	18.13±0.24
3FGL J0707.2+6101	18.05±0.02	17.42±0.02	16.95±0.03	16.6±0.06	20.01±0.11	20.05±0.15	19.42±0.12	18.98±0.12	18.22±0.1	17.99±0.16
4FGL J0800.9+4401	19.09±0.05	18.57±0.05	18.4±0.1	18.59±0.36	>21.58	>21.11	20.48±0.29	19.83±0.28	19.23±0.32	>18.52
3FGL J0103.4+5336	18.45±0.12	17.82±0.06	17.5±0.05	17.2±0.09	19.89±0.16	20.57±0.28	20.12±0.22	19.26±0.13	18.62±0.11	17.93±0.11
3FGL J1138.2+4905	20.88±0.29	20.22±0.31	>20.54	>19.56	>23.24	>22.73	22.57±0.36	>21.84	>21.05	>20.0
3FGL J1323.9+1405	18.07±0.02	17.8±0.03	17.64±0.05	17.56±0.16	18.97±0.07	18.62±0.08	18.47±0.08	18.07±0.07	18.14±0.1	17.71±0.14
3FGL J1354.5+3705	17.99±0.02	17.48±0.02	17.07±0.03	16.64±0.06	19.46±0.06	19.13±0.07	19.06±0.08	18.49±0.06	18.13±0.07	17.83±0.1
3FGL J1500.6+4750	19.78±0.23	19.73±0.29	20.25±0.73	>19.27	21.55±0.34	>20.5	20.56±0.24	20.12±0.27	>19.79	18.03±0.27
3FGL J1649.4+5238	17.54±0.01	17.12±0.02	16.67±0.02	16.26±0.05	18.94±0.08	18.81±0.09	18.61±0.09	18.0±0.08	17.65±0.08	17.18±0.11
3FGL J1702.6+3116	18.29±0.03	18.01±0.03	17.9±0.06	18.4±0.29	19.58±0.09	19.38±0.1	19.2±0.1	18.75±0.09	18.36±0.1	18.56±0.21

Table 3. SED fitting

3FGL or 3FHL Name	$z_{\text{phot,best}}^a$	$z_{\text{spec,4LAC}}^b$	$z_{\text{spec,SDSS}}^b$	Power Law Template				Galaxy Template			
				z_{phot}^c	$\chi^2 d$	P_z^e	β^f	z_{phot}^c	$\chi^2 d$	P_z^e	Model
Sources with confirmed photometric redshifts											
4FGL J0506.9+0323	$2.03_{-0.05}^{+0.07}$	$2.03_{-0.05}^{+0.07}$	19.1	96.7	0.0	$1.13_{-0.01}^{+0.01}$	15.4	79.5	pl_QSOH_template_norm.sed
4FGL J1125.1-2101	$1.84_{-0.03}^{+0.10}$	$1.84_{-0.03}^{+0.10}$	23.6	99.5	0.0	$1.28_{-0.03}^{+0.00}$	22.5	93.7	pl_QSO_DR2_029_t0.spec
4FGL J1823.5+6858	$2.04_{-0.14}^{+0.16}$	$2.04_{-0.14}^{+0.16}$	4.0	93.1	1.45	$2.13_{-0.06}^{+0.04}$	10.6	93.4	pl_QSOH_template_norm.sed
4FGL J2144.2+3132	$2.93_{-0.04}^{+0.01}$	$2.93_{-0.04}^{+0.01}$	20.6	100.0	0.8	$0.04_{-0.01}^{+0.01}$	12.2	98.8	S0_70_QSO2_30.sed
Sources with photometric redshift upper limits											
4FGL J0019.6+2022	< 3.56	$3.23_{-0.49}^{+0.33}$	0.6	75.9	1.45	$0.20_{-0.20}^{+0.06}$	0.1	59.3	S0_90_QSO2_10.sed
4FGL J0023.9+1603	< 3.55	$3.14_{-0.16}^{+0.41}$	1.0	69.9	1.15	$0.09_{-0.05}^{+0.13}$	0.0	29.9	S0_70_QSO2_30.sed
4FGL J0026.6-4600	$1.01_{-1.01}^{+0.20}$	38.9	33.5	0.85	$0.00_{-0.00}^{+0.01}$	38.3	14.3	pl_I22491_30_TQSO1_70.sed
3FHL J0121.8+3808	< 0.99	$0.12_{-0.12}^{+0.87}$	4.7	22.1	0.5	$0.16_{-0.13}^{+0.40}$	2.8	42.3	pl_TQSO1_template_norm.sed
4FGL J0125.3-2548	< 1.37	$1.00_{-1.00}^{+0.37}$	17.3	27.3	1.95	$0.00_{-0.00}^{+0.07}$	19.0	42.4	Mrk231_template_norm.sed
4FGL J0138.0+2247	$1.38_{-0.01}^{+0.00}$	220.9	98.6	3.0
4FGL J0139.0+2601	< 1.13	$0.87_{-0.87}^{+0.26}$	4.2	32.7	1.5	$0.00_{-0.00}^{+0.01}$	12.2	99.0	I22491_90_TQSO1_10.sed
4FGL J0144.6+2705	< 2.85	$2.62_{-0.00}^{+0.23}$	4.6	81.5	2.0	$0.06_{-0.06}^{+0.04}$	7.0	62.6	S0_60_QSO2_40.sed
4FGL J0156.9-5301	< 0.89	$0.24_{-0.24}^{+0.65}$	9.8	27.2	1.1	$0.00_{-0.00}^{+0.30}$	5.9	28.8	I22491_50_TQSO1_50.sed
4FGL J0237.3+2000	< 1.46	$1.23_{-1.23}^{+0.23}$	2.0	33.4	1.0	$1.24_{-0.08}^{+0.12}$	2.9	80.3	pl_QSOH_template_norm.sed
4FGL J0338.5+1302	< 1.84	$1.73_{-0.97}^{+0.11}$	12.2	29.5	0.3	$1.10_{-0.11}^{+0.34}$	11.0	65.9	pl_QSOH_template_norm.sed
4FGL J0344.4+3432	< 2.26	$1.12_{-1.12}^{+1.14}$	6.3	17.6	2.0	$1.47_{-1.47}^{+0.01}$	8.4	27.7	Sey2_template_norm.sed
4FGL J0406.0-5407	< 1.1	$0.03_{-0.03}^{+1.07}$	16.4	12.7	1.65	$0.46_{-0.46}^{+0.06}$	25.3	56.4	Spi4_template_norm.sed
4FGL J0439.8-1859	< 1.07	$0.85_{-0.85}^{+0.22}$	12.3	32.2	1.1	$0.00_{-0.00}^{+0.03}$	14.1	97.8	I22491_60_TQSO1_40.sed
4FGL J0500.6-4911	$0.93_{-0.93}^{+0.26}$	32.2	32.2	1.3	$0.08_{-0.02}^{+0.02}$	34.8	98.1	I22491_80_TQSO1_20.sed
4FGL J0551.0-1622
4FGL J0558.8-7459	< 1.85	$1.58_{-0.14}^{+0.27}$	2.7	75.2	1.65	$1.83_{-1.83}^{+0.11}$	6.5	73.9	pl_QSOH_template_norm.sed
4FGL J0700.5-6610	< 1.08	$0.81_{-0.81}^{+0.27}$	5.4	31.9	1.4	$0.00_{-0.00}^{+0.01}$	7.3	99.8	I22491_80_TQSO1_20.sed
4FGL J0746.6-4754	< 1.21	$1.00_{-1.00}^{+0.21}$	1.4	34.9	0.95	$0.01_{-0.01}^{+0.03}$	6.1	87.1	I22491_40_TQSO1_60.sed
4FGL J0816.9+2050
3FGL J0851.8+5531	< 1.21	$1.03_{-1.03}^{+0.18}$	4.5	32.2	1.25	$0.03_{-0.03}^{+0.06}$	12.3	92.2	I22491_70_TQSO1_30.sed
4FGL J0854.3+4408	< 1.14	$0.96_{-0.96}^{+0.18}$	0.4	32.7	0.8	$0.01_{-0.01}^{+0.02}$	4.2	71.7	pl_I22491_30_TQSO1_70.sed
4FGL J0859.4+6218	< 1.1	$0.04_{-0.04}^{+1.06}$	0.6	12.8	1.2	$0.00_{-0.00}^{+0.04}$	1.6	73.6	I22491_60_TQSO1_40.sed
4FGL J0910.6+3329	< 1.17	$1.03_{-1.03}^{+0.14}$	1.8	32.8	0.9	$0.00_{-0.00}^{+0.02}$	6.1	90.7	I22491_40_TQSO1_60.sed
4FGL J0910.6+3329	< 4.0	$2.73_{-0.27}^{+1.27}$	0.0	44.7	2.0	$0.09_{-0.09}^{+3.91}$	0.0	9.4	S0_70_QSO2_30.sed
4FGL J1019.7+6321	< 1.15	$0.85_{-0.85}^{+0.30}$	13.3	30.4	1.25	$0.00_{-0.00}^{+0.02}$	11.3	87.2	I22491_70_TQSO1_30.sed
4FGL J1059.2-1134	$0.25_{-0.25}^{+0.59}$	32.1	29.7	1.65	$0.00_{-0.00}^{+0.03}$	19.9	71.5	I22491_90_TQSO1_10.sed
4FGL J1248.3+5820	< 1.06	$0.58_{-0.58}^{+0.48}$	0.3	29.0	1.2	$0.00_{-0.00}^{+0.02}$	3.9	94.1	I22491_60_TQSO1_40.sed
4FGL J1259.8-3749	$1.14_{-0.08}^{+0.00}$	90.5	39.9	3.0	$3.96_{-0.00}^{+0.04}$	251.6	100.0	pl_QSO_DR2_029_t0.spec
4FGL J1304.9-2107	< 1.06	$0.73_{-0.73}^{+0.33}$	1.1	27.7	1.5	$0.13_{-0.13}^{+0.58}$	0.1	33.5	CB1_0_LOIII4.sed
4FGL J1307.6-4259	< 1.34	$1.07_{-0.32}^{+0.27}$	6.1	37.9	1.1	$0.00_{-0.00}^{+0.01}$	12.7	45.5	I22491_60_TQSO1_40.sed

Table 3 continued on next page

Table 3 (continued)

3FGL or 3FHL Name	$z_{\text{phot,best}}^a$	$z_{\text{spec,4LAC}}^b$	$z_{\text{spec,SDSS}}^b$	Power Law Template				Galaxy Template			
				z_{phot}^c	$\chi^2{}^d$	P_z^e	β^f	z_{phot}^c	$\chi^2{}^d$	P_z^e	Model
4FGL J1427.6–3305	$1.53_{-0.15}^{+0.12}$	72.1	78.0	2.0	$0.46_{-0.04}^{+0.04}$	10.5	98.9	Sey2_template_norm.sed
4FGL J1516.8+3651	< 2.15	$1.87_{-0.27}^{+0.28}$	2.4	82.6	1.9	$0.01_{-0.01}^{+0.01}$	4.6	83.3	S0_80-QSO2_20.sed
4FGL J1612.4–3100	< 1.39	$0.98_{-0.98}^{+0.41}$	8.0	26.6	1.5	$0.16_{-0.06}^{+0.06}$	7.1	85.4	Spi4_template_norm.sed
4FGL J1624.6+5651	< 1.16	$0.96_{-0.96}^{+0.20}$	13.3	30.9	1.3	$0.00_{-0.00}^{+0.01}$	15.7	90.6	I22491_70_TQSO1_30.sed
4FGL J1707.1–1931	$4.00_{-0.18}^{+0.00}$	0.1	62.1	pl_QSOH_template_norm.sed
4FGL J1754.2+3212	< 1.1	$0.82_{-0.82}^{+0.28}$	1.4	31.7	1.05	$0.00_{-0.00}^{+0.03}$	4.3	89.7	I22491_50_TQSO1_50.sed
3FGL J1829.4+5402	< 1.3	$1.14_{-0.30}^{+0.16}$	1.0	39.6	1.0	$0.00_{-0.00}^{+0.03}$	6.8	74.6	I22491_50_TQSO1_50.sed
4FGL J1836.4+3137	< 1.15	$0.87_{-0.87}^{+0.28}$	10.2	30.6	1.8	$0.00_{-0.00}^{+0.03}$	11.1	57.4	Sey18_template_norm.sed
4FGL J1838.8+4802	< 1.13	$0.92_{-0.92}^{+0.21}$	1.1	35.2	0.85	$0.01_{-0.01}^{+0.02}$	5.3	84.5	pl_I22491_30_TQSO1_70.sed
3FGL J1926.8+6154	< 1.14	$0.93_{-0.93}^{+0.21}$	1.6	32.5	0.7	$0.03_{-0.02}^{+0.21}$	3.7	27.8	pl_I22491_10_TQSO1_90.sed
4FGL J1946.0–3112	< 1.48	$1.38_{-0.11}^{+0.10}$	15.3	70.4	1.2	$0.10_{-0.05}^{+0.05}$	15.5	95.4	Spi4_template_norm.sed
4FGL J1959.7–4725	< 1.06	$0.26_{-0.26}^{+0.80}$	4.6	23.1	1.05	$0.00_{-0.00}^{+0.01}$	5.9	89.7	I22491_50_TQSO1_50.sed
4FGL J2030.9+1935	< 0.96	$0.03_{-0.03}^{+0.93}$	8.0	14.6	1.05	$0.04_{-0.04}^{+0.09}$	6.7	82.9	I22491_50_TQSO1_50.sed
4FGL J2126.1–3922	< 2.1	$1.77_{-0.43}^{+0.33}$	0.3	63.6	1.45	$1.83_{-0.53}^{+0.02}$	2.4	45.5	pl_QSOH_template_norm.sed
4FGL J2149.6+0323	< 1.34	$1.15_{-0.57}^{+0.19}$	0.5	37.5	1.4	$0.00_{-0.00}^{+0.02}$	9.9	93.7	I22491_90_TQSO1_10.sed
4FGL J2243.7–1231	< 1.05	$0.03_{-0.03}^{+1.02}$	2.5	13.2	0.75	$0.53_{-0.53}^{+0.09}$	1.4	58.3	pl_QSOH_template_norm.sed
4FGL J2243.9+2021	< 1.18	$1.00_{-1.00}^{+0.18}$	0.3	36.9	0.95	$0.01_{-0.01}^{+0.02}$	5.9	94.4	I22491_40_TQSO1_60.sed
4FGL J2325.6+1644	< 1.04	$0.03_{-0.03}^{+1.01}$	4.7	13.7	0.9	$0.18_{-0.18}^{+0.06}$	3.0	56.8	I22491_40_TQSO1_60.sed
4FGL J2352.0+1750	< 1.53	$1.34_{-0.19}^{+0.19}$	9.3	59.3	0.95	$1.29_{-0.08}^{+0.06}$	7.2	99.8	pl_QSOH_template_norm.sed
3FHL J2358.4–1808	< 1.11	$0.85_{-0.85}^{+0.26}$	6.3	31.6	1.25	$0.00_{-0.00}^{+0.01}$	6.4	98.0	I22491_70_TQSO1_30.sed
3FGL J0707.2+6101	< 1.25	$1.06_{-1.06}^{+0.19}$	11.0	36.1	2.0	$0.00_{-0.00}^{+0.02}$	19.2	95.8	Mrk231_template_norm.sed
4FGL J0800.9+4401	< 2.13	$1.90_{-0.21}^{+0.23}$	4.0	83.9	1.3	$0.02_{-0.02}^{+0.02}$	8.7	21.5	S0_90-QSO2_10.sed
3FGL J0103.4+5336	< 1.05	$0.04_{-0.04}^{+1.01}$	14.0	12.8	2.0	$0.07_{-0.04}^{+0.04}$	3.7	99.9	Mrk231_template_norm.sed
3FGL J1138.2+4905	$2.64_{-0.18}^{+0.24}$	8.5	81.5	Mrk231_template_norm.sed
3FGL J1323.9+1405	< 1.38	$1.24_{-0.13}^{+0.14}$	3.1	68.9	0.65	$1.21_{-0.09}^{+0.07}$	3.6	92.2	pl_I22491_30_TQSO1_70.sed
3FGL J1354.5+3705	< 1.0	$0.24_{-0.24}^{+0.76}$	4.5	24.4	1.65	$0.00_{-0.00}^{+0.01}$	18.9	76.4	I22491_90_TQSO1_10.sed
3FGL J1500.6+4750	< 2.06	$1.84_{-0.31}^{+0.22}$	10.5	65.9	0.25	$1.40_{-0.40}^{+0.11}$	11.1	56.8	pl_QSO_DR2_029_t0.spec
3FGL J1649.4+5238	< 1.02	$0.12_{-0.12}^{+0.90}$	2.8	21.5	1.6	$0.00_{-0.00}^{+0.03}$	11.4	92.2	I22491_90_TQSO1_10.sed
3FGL J1702.6+3116	< 1.45	$1.27_{-0.22}^{+0.18}$	15.3	52.4	0.9	$1.23_{-0.06}^{+0.07}$	13.9	98.9	pl_QSOH_template_norm.sed

^a Best-fit or upper limit of the photometric redshift, either a value or an upper limit.

^b The spectroscopic redshifts are extracted from Ajello et al. (2020), Abazajian et al. (2009) and Marchesini et al. (2019) unless specifically denoted.

^c Photometric redshifts with 1σ confidence level.

^d χ^2 value for ten degrees of freedom.

^e Redshift probability density at $z_{\text{phot}} \pm 0.1 (1 + z_{\text{phot}})$.

^f Spectral slope for the power-law model of the form $F_{\lambda} \propto \lambda^{-\beta}$.

5. RESULTS

We measured photometric redshifts for 64 sources. The Table 3 reports the photometric redshifts or upper limits, fitting statistics, and the corresponding SED models for the sample. Four high- z BL Lacs are reported, and detailed information about the models and magnitudes is presented in Figure 2. The four high- z BL Lacs are 4FGL J0506.9+0323, 4FGL J1125.1–2101, 4FGL J1823.5+6858, 4FGL J2144.2+3132. The power-law templates estimates redshifts at $2.03_{-0.05}^{+0.07}$, $1.84_{-0.03}^{+0.10}$, $2.04_{-0.14}^{+0.16}$, $2.93_{-0.04}^{+0.01}$ respectively, while galaxy templates estimates redshifts at $1.13_{-0.06}^{+0.01}$, $1.28_{-0.03}^{+0.00}$, $2.13_{-0.06}^{+0.04}$, $0.04_{-0.01}^{+0.01}$ respectively. However, all the high- z sources are identified as BL Lacs in the 4FGL-DR3 catalog, therefore the redshifts determined by the power-law models

are more likely, and they are reported as the best-fit photometric in Table 3. Upper limits are also reported for sources with $P_z < 90\%$ and $\chi^2 \leq 30$.

Truebenbach & Darling (2017) measured the redshift of 4FGL J1823.5+6858 at 2.14 ± 10^{-3} , which is compatible with our result at $2.04^{+0.16}_{-0.14}$. Domínguez et al. (2024a) provides the redshift upper limits of blazars from the extragalactic background light attenuation. The photometric redshift of 4FGL J1125.1–2101, $1.84^{+0.10}_{-0.03}$, is compatible with the upper limit $< 1.76^{+0.90}_{-0.62}$ from Domínguez et al. (2024a). Another source, 4FGL J2144.2+3132, has a photometric redshift at $2.93^{+0.01}_{-0.04}$, while the upper limit is $< 0.79^{+0.78}_{-0.74}$ from Domínguez et al. (2024a).

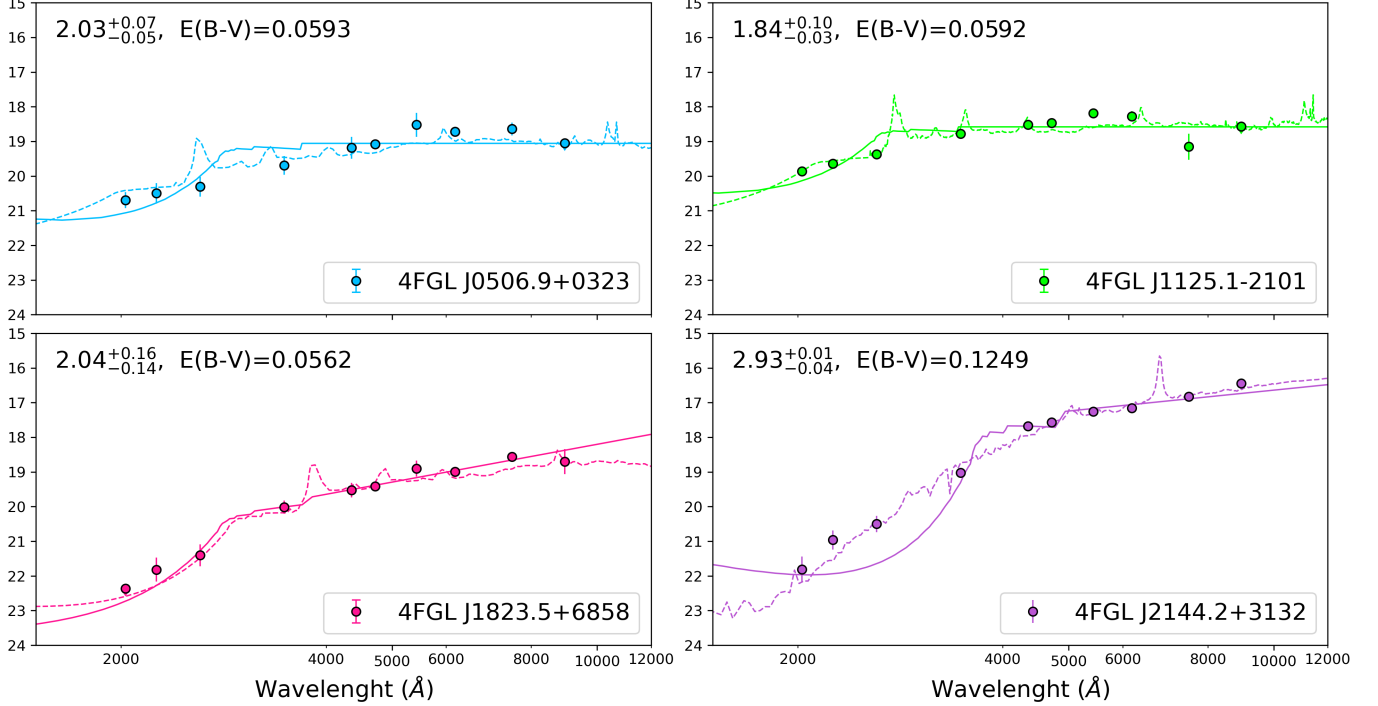


Figure 2. The SEDs of the four high-redshift BL Lacs. The solid circles with black edges are photometric data from Table 3. The magnitudes are ordered in the following the central wavelength of the filters: $uw2$, $um2$, $uw1$, uuu , ubb , g' , uvv , r' , i' , z' . The solid line represents power-law model while dashed line represents galaxy model.

6. DISCUSSIONS

6.1. Cosmic Gamma-ray Horizon

The extragalactic background light (EBL) interacts with the very-high-energy (VHE) photon (>100 GeV) from the blazars. The EBL photons from ultraviolet to infrared band annihilate with the VHE photons, restraining the travel of VHE photon in the universe. Therefore, there is a redshift-dependent opacity for VHE photons to each us (Finke et al. 2010; Domínguez et al. 2011), which is called the cosmic gamma-ray horizon (CGRH, Domínguez et al. (2013)).

Figure 3 shows the EBL model (Domínguez et al. 2024b; Finke et al. 2022; Saldana-Lopez et al. 2021) plotted with 4LAC blazars, blazars with spectroscopic redshifts, and the high- z BL Lacs found by the Photo-z campaign. The high- z BL Lacs increased the population of the sources on the high-redshift side in the CGRH plot, thus constraining the EBL model where data points are scarce.

6.2. Blazar Sequence

A unified blazar model, blazar sequence, is proposed by Fossati et al. (1998) to explain the population of blazars. Blazars are separated into two groups, BL Lac and FSRQ, by their spectral properties: the synchrotron peak frequency at rest frame ($\nu_{\text{pk, rest}}^{\text{sy}}$) versus synchrotron peak luminosity ($L_{\text{pk}}^{\text{sy}}$), Compton dominance (CD), and gamma-ray index (Γ_γ). Compton dominance is the ratio between the inverse-Compton luminosity ($L_{\text{pk}}^{\text{IC}}$) to $L_{\text{pk}}^{\text{sy}}$. The blazar sequence predicts that $\nu_{\text{pk, rest}}^{\text{sy}}$ is anti-correlated

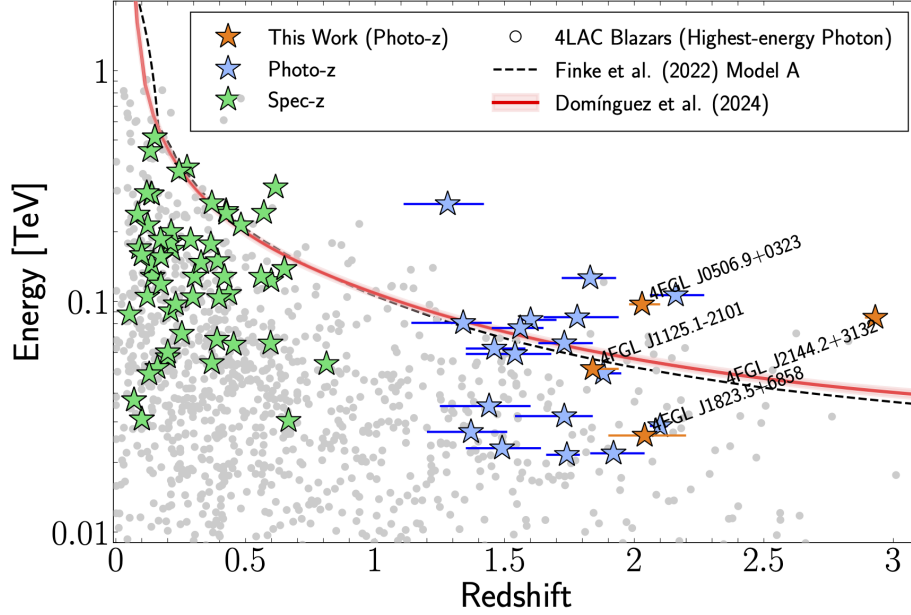


Figure 3. The cosmic gamma-ray horizon plot. The grey circles are from the 4LAC blazars. The blue and orange stars are the high- z BL Lacs found by the Photo- z campaign (Rau et al. 2012; Kaur et al. 2017; Kaur et al. 2018; Rajagopal et al. 2020; Sheng et al. 2024) including this work. Note that only high- z BL Lac reported with highest energy photon (HEP) are plotted here. The green stars are BL Lacs with spectroscopic redshift determined by Marchesi et al. (2018); Desai et al. (2019); Paiano et al. (2020); Rajagopal et al. (2021); Goldoni et al. (2021); García-Pérez et al. (2023); Kasai et al. (2023).

with $L_{\text{pk}}^{\text{sy}}$, Compton dominance, and Γ_{γ} . BL Lacs dominates areas with higher $v_{\text{pk, rest}}^{\text{sy}}$, lower $L_{\text{pk}}^{\text{sy}}$, Compton dominance, and gamma-ray index. The FSRQ population shows the opposite relation: they have lower $v_{\text{pk, rest}}^{\text{sy}}$, higher $L_{\text{pk}}^{\text{sy}}$, Compton dominance, and gamma-ray index. Figure 4(a), 4(b), and 4(c) show how the anti-correlation of the spectral properties divides blazars into two population groups. However, the blazar sequence can be caused by some selection effects (Giommi et al. 2012). Figure 4(a) shows a disagreement with the current blazar sequence model. The luminous high- z BL Lacs are found by the Photo- z campaign. Therefore, our high- z BL Lacs are essential to study the blazar population from an unbiased perspective.

Most of the spectral properties are calculated using the 4LAC catalog. We also utilized two additional methods if the 4LAC catalog does not have the spectral values needed for the calculation. We use the SDSS Sky Explorer⁵ to plot the SED and fit the synchrotron and inverse-Compton peak. In addition, we also calculate the inverse-Compton peak for power-law-like spectra (Marcotulli et al. 2020) using:

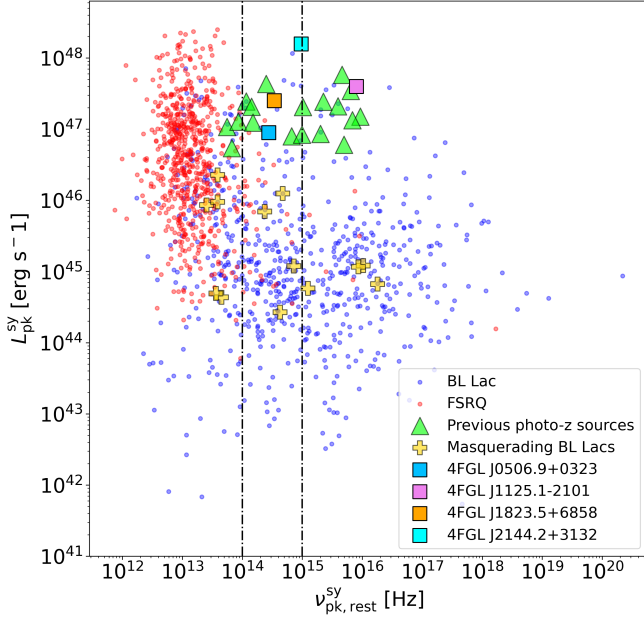
$$\frac{dN}{dE} = K \left[\left(\frac{E}{E_b} \right)^{\delta_1} + \left(\frac{E}{E_b} \right)^{\delta_2} \right]^{-1}. \quad (2)$$

The break energy E_b is found by the $E_b - \Gamma$ relationship in Ajello et al. (2015). The K is normalized to the flux integrated from 1 to 100 GeV in the 4FGL catalog.

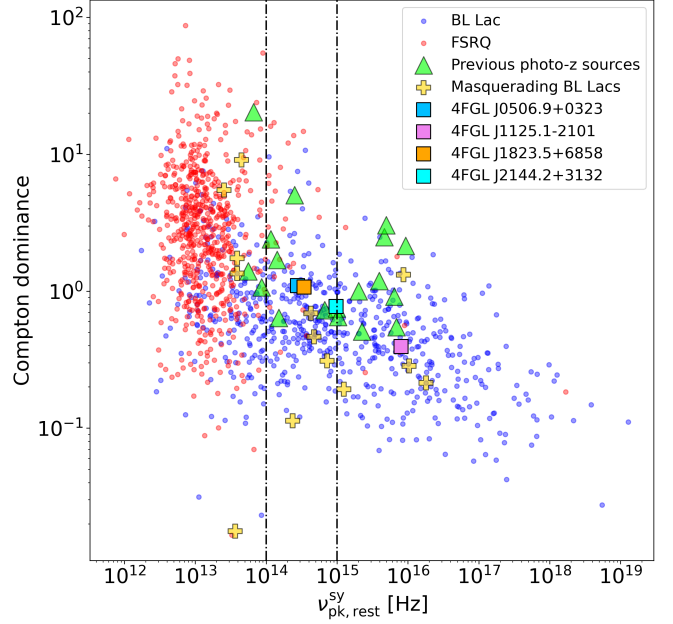
6.3. The Fermi Blazar Divide

The Fermi blazar divide is found by Ghisellini et al. (2009), which separates the blazar population into BL Lac and FSRQ by gamma-ray luminosity (L_{γ}) and gamma-ray index (Γ_{γ}): BL Lacs dominates the area with the lower gamma-ray luminosity ($L_{\gamma} < 10^{47}$ erg s $^{-1}$) and harder spectra index ($\Gamma_{\gamma} < 2.2$) in the $\Gamma_{\gamma} - L_{\gamma}$ space. Figure 4(d) shows the Fermi blazar divide and the high- z BL Lacs discovered by the Photo- z campaign, using the 4LAC catalog data (Ajello et al. 2020). We utilized the same method in Sheng et al. (2024) to calculate the gamma-ray luminosity from 0.1 GeV to 100 GeV. The plot indicates the distinct separation between the FSRQ and BL Lac populations. However, the high- z BL Lacs found by our photometric method stand out from the two groups in the plot: they are luminous BL Lacs with harder spectra. These outliers can be explained by the "blue

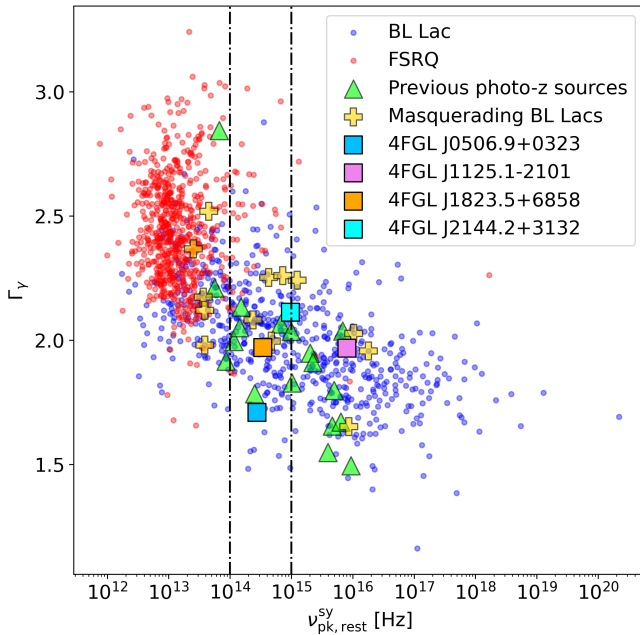
⁵ <https://tools.ssdc.asi.it/>



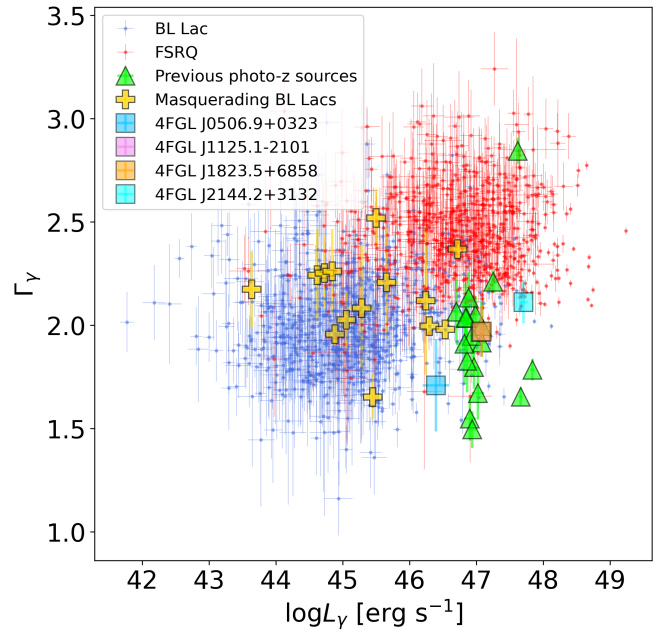
(a) Synchrotron peak luminosity vs. rest-frame synchrotron peak frequency.



(b) Compton dominance vs. synchrotron peak frequency at rest frame.



(c) Gamma-ray index vs. synchrotron peak frequency at rest frame.



(d) Gamma-ray index vs. gamma-ray luminosity (0.1-100 GeV).

Figure 4. The colored dots are calculated from the 4LAC catalog (Ajello et al. 2020). The triangles are the previous high- z BL Lacs (Rau et al. 2012; Kaur et al. 2017; Kaur et al. 2018; Rajagopal et al. 2020), while the squares are the ones found in this work. The vertical dotted lines divides the blazars to LSP, ISP, and HSP groups. The orange crosses are the masquerading BL Lacs from Padovani et al. (2022); Paiano et al. (2023); Sahakyan et al. (2023). The indices are not corrected for EBL absorption.

quasars” or “masquerading BL Lacs” proposed by Giommi et al. (2013). Masquerading BL Lacs are FSRQs classified as BL Lacs because the luminous synchrotron emission from the jet saturates the emission lines from the host galaxy.

We also calculated the disk-to-Eddington luminosity ratio following the same assumption and method in Sheng et al. (2024). The four high- z BL Lacs, 4FGL J0506.9+0323, 4FGL J1125.1–2101, 4FGL J1823.5+6858, 4FGL J2144.2+3132, have ratios

of 0.008, 0.037, 0.039, 0.147 respectively. Three of them show efficient accretion from disk (ratio > 0.02), indicating the fingerprints of FSRQ. Figure 4(d) shows that the Photo-z campaign can efficiently reveal potential masquerading BL Lacs.

7. SUMMARY AND CONCLUSIONS

This work measures the photometric redshifts for 64 blazars, among which 59 are BL Lacs and 5 are blazar candidates of uncertain type (BCU). The sources are observed in ten filters by the *Swift* observatory and SARA-CT/RM telescopes. The photometric data are produced via the automatic pipeline set up by the *photozpy* package. Following the method implemented in Rau et al. (2012), we obtained redshifts ($z > 1.3$) for 4 BL Lacs and upper limits for 50 sources. So far, the Photo-z campaign has discovered 23 high- z BL Lacs, including this work. The rare high- z BL Lacs are essential probes for the EBL models and blazar population. Our sample examines the cosmic gamma-ray horizon: the two high- z sources that lie above the horizon might indicate that the current EBL model might be too opaque. In addition, our work also shows that the blazar sequence might be subject to selection effects due to the challenges in the BL Lac redshift measurement. Figure 4(a) demonstrates that the missing luminous high- z BL Lacs are found by our method. Moreover, our high- z BL Lacs are potential masquerading BL Lacs due to their high luminosity and hard spectra. Three high- z sources found in this paper show efficient disk accretion, indicating that they might be FSRQs whose broad-line emission is outshone by the luminous non-thermal emission from the jet.

REFERENCES

- Abazajian, K. N., Adelman-McCarthy, J. K., Agüeros, M. A., et al. 2009, *ApJS*, 182, 543
- Abdo, A. A., Ackermann, M., Ajello, M., et al. 2010, *The Astrophysical Journal*, 723, 1082
- Abdollahi, S., Ackermann, M., Atwood, W., et al. 2018
- Abdollahi, S., Acero, F., Ackermann, M., et al. 2020, *The Astrophysical Journal Supplement Series*, 247, 33
- Abdollahi, S., Acero, F., Baldini, L., et al. 2022, *The Astrophysical Journal Supplement Series*, 260, 53
- Acero, F., Ackermann, M., Ajello, M., et al. 2015, *The Astrophysical Journal Supplement Series*, 218, 23
- Ackermann, M., Ajello, M., Allafort, A., et al. 2011, *The Astrophysical Journal*, 743, 171
- . 2012, *Science*, 338, 1190
- Ajello, M., Romani, R. W., Gasparrini, D., et al. 2013, *The Astrophysical Journal*, 780, 73
- Ajello, M., Gasparrini, D., Sánchez-Conde, M., et al. 2015, *ApJL*, 800, L27
- Ajello, M., Atwood, W., Baldini, L., et al. 2017, *The Astrophysical Journal Supplement Series*, 232, 18
- Ajello, M., Angioni, R., Axelsson, M., et al. 2020, *The Astrophysical Journal*, 892, 105
- Ajello, M., Baldini, L., Ballet, J., et al. 2022, *The Astrophysical Journal Supplement Series*, 263, 24
- Albareti, F. D., Allende Prieto, C., Almeida, A., et al. 2017, *The Astrophysical Journal Supplement Series*, 233, 25, aDS Bibcode: 2017ApJS..233...25A
- Arnouts, S., Cristiani, S., Moscardini, L., et al. 1999, *Monthly Notices of the Royal Astronomical Society*, 310, 540
- Beroiz, M., Cabral, J., & Sanchez, B. 2020, *Astronomy and Computing*, 32, 100384
- Biteau, J., & Williams, D. A. 2015, *The Astrophysical Journal*, 812, 60
- Blandford, R. D., & Rees, M. J. 1978, *Physica Scripta*, 17, 265
- Bohlin, R. C., Colina, L., & Finley, D. S. 1995, *The Astronomical Journal*, 110, 1316
- Bradley, L., Sipőcz, B., Robitaille, T., et al. 2024, *astropy/photutils*: 1.12.0, doi:10.5281/zenodo.10967176
- Carini, M., Miller, H., Noble, J., & Sadun, A. 1991, *The Astronomical Journal*, 101, 1196
- Chabrier, G., Baraffe, I., Allard, F., & Hauschildt, P. 2000, *The Astrophysical Journal*, 542, 464
- Craig, M., Crawford, S., Seifert, M., et al. 2017, *astropy/ccdproc*: v1.3.0.post1, doi:10.5281/zenodo.1069648
- Dermer, C. D., & Schlickeiser, R. 1994, *ApJS*, 90, 945
- Desai, A., Marchesi, S., Rajagopal, M., & Ajello, M. 2019, *The Astrophysical Journal Supplement Series*, 241, 5
- Domínguez, A., & Ajello, M. 2015, *The Astrophysical Journal*, 813, L34
- Domínguez, A., Finke, J. D., Prada, F., et al. 2013, *The Astrophysical Journal*, 770, 77
- Domínguez, A., Primack, J. R., Rosario, D. J., et al. 2011, *MNRAS*, 410, 2556
- Domínguez, A., Láinez, M., Paliya, V. S., et al. 2024a, *Monthly Notices of the Royal Astronomical Society*, 527, 4763
- Domínguez, A., Østergaard Kirkeberg, P., Wojtak, R., et al. 2024b, *Monthly Notices of the Royal Astronomical Society*, 527, 4632
- Fabian, A. C. 2008, *AIP Conference Proceedings*, 254, 657
- Finke, J. D., Ajello, M., Domínguez, A., et al. 2022, *The Astrophysical Journal*, 941, 33
- Finke, J. D., Razzaque, S., & Dermer, C. D. 2010, *ApJ*, 712, 238

- Fossati, G. a., Maraschi, L., Celotti, A., Comastri, A., & Ghisellini, G. 1998, *Monthly Notices of the Royal Astronomical Society*, 299, 433
- Franceschini, A., & Rodighiero, G. 2017, *Astronomy & Astrophysics*, 603, A34
- García-Pérez, A., Peña-Herazo, H. A., Massaro, F., et al. 2023, *The Astronomical Journal*, 165, 127
- Gehrels, N., Chincarini, G., Giommi, P. e., et al. 2004, *The Astrophysical Journal*, 611, 1005
- Ghisellini, G., Maraschi, L., & Tavecchio, F. 2009, *Monthly Notices of the Royal Astronomical Society: Letters*, 396, L105
- Giommi, P., Padovani, P., & Polenta, G. 2013, *Monthly Notices of the Royal Astronomical Society*, 431, 1914
- Giommi, P., Padovani, P., Polenta, G., et al. 2012, *Monthly Notices of the Royal Astronomical Society*, 420, 2899
- Goldoni, P., Pita, S., Boisson, C., et al. 2021, *Astronomy & Astrophysics*, 650, A106
- Greiner, J., Bornemann, W., Clemens, C., et al. 2007, *The ESO Messenger*, 130, 12
- Hogg, D. W., Blanton, M., Lang, D., Mierle, K., & Roweis, S. 2008, 394, 27
- Ilbert, O., Arnouts, S., McCracken, H., et al. 2006, *Astronomy & Astrophysics*, 457, 841
- Joffre, S., Silver, R., Rajagopal, M., et al. 2022, *The Astrophysical Journal*, 940, 139
- Kasai, E., Goldoni, P., Pita, S., et al. 2023, *Monthly Notices of the Royal Astronomical Society*, 518, 2675
- Kataoka, J., Madejski, G., Sikora, M., et al. 2008, *The Astrophysical Journal*, 672, 787, publisher: American Astronomical Society
- Kaur, A., Rau, A., Ajello, M., et al. 2018, *ApJ*, 859, 80
- Kaur, A., Rau, A., Ajello, M., et al. 2017, *ApJ*, 834, 41
- Keel, W. C., Oswalt, T., Mack, P., et al. 2016, *Publications of the Astronomical Society of the Pacific*, 129, 015002, publisher: IOP Publishing
- Kerby, S., Kaur, A., Falcone, A. D., et al. 2021, *The Astronomical Journal*, 161, 154
- Krübler, T., Schady, P., Greiner, J., et al. 2011, *A&A*, 526, A153
- Landolt, A. U. 2009, *The Astronomical Journal*, 137, 4186, aDS Bibcode: 2009AJ....137.4186L
- Lang, D., Hogg, D. W., Mierle, K., Blanton, M., & Roweis, S. 2010, *The Astronomical Journal*, 139, 1782
- Maraschi, L., Ghisellini, G., & Celotti, A. 1994, 159, 221
- Marchesi, S., Kaur, A., & Ajello, M. 2018, *The Astronomical Journal*, 156, 212
- Marchesini, E. J., Peña-Herazo, H., Álvarez Crespo, N., et al. 2019, *Astrophysics and Space Science*, 364, 1
- Marconi, A., Risaliti, G., Gilli, R., et al. 2004, *Monthly Notices of the Royal Astronomical Society*, 351, 169
- Marcotulli, L., Di Mauro, M., & Ajello, M. 2020, *ApJ*, 896, 6
- Marcotulli, L., Paliya, V. S., Ajello, M., et al. 2017, *The Astrophysical Journal*, 839, 96
- Moralejo, A., Domínguez, A., Ramazani, V. F., et al. 2017, arXiv:1709.02238 [astro-ph], arXiv:1709.02238
- Otero-Santos, J., Acosta-Pulido, J., Becerra González, J., et al. 2022, *Monthly Notices of the Royal Astronomical Society*, 511, 5611
- Padovani, P., & Giommi, P. 1995, *The Astrophysical Journal*, 444, 567
- Padovani, P., Giommi, P., Falomo, R., et al. 2022, *MNRAS*, 510, 2671
- Paiano, S., Falomo, R., Franceschini, A., Treves, A., & Scarpa, R. 2017, *The Astrophysical Journal*, 851, 135
- Paiano, S., Falomo, R., Treves, A., et al. 2023, *Monthly Notices of the Royal Astronomical Society*, 521, 2270
- Paiano, S., Falomo, R., Treves, A., & Scarpa, R. 2020, *Monthly Notices of the Royal Astronomical Society*, 497, 94
- Perlman, E. S. 2013, in *Planets, Stars and Stellar Systems: Volume 6: Extragalactic Astronomy and Cosmology*, ed. T. D. Oswalt & W. C. Keel (Dordrecht: Springer Netherlands), 305–386
- Pickles, A. 1998, *Publications of the Astronomical Society of the Pacific*, 110, 863
- Poole, T. S., Breeveld, A. A., Page, M. J., et al. 2008, *Monthly Notices of the Royal Astronomical Society*, 383, 627, aDS Bibcode: 2008MNRAS.383..627P
- Prandini, E., & Ghisellini, G. 2022, *Galaxies*, 10, 35
- Racine, R. 1970, *The Astrophysical Journal*, 159, L99
- Rajagopal, M., Kaur, A., Ajello, M., et al. 2020, *The Astrophysical Journal*, 898, 18
- Rajagopal, M., Marchesi, S., Kaur, A., et al. 2021, *The Astrophysical Journal Supplement Series*, 254, 26
- Rau, A., Schady, P., Greiner, J., et al. 2012, *Astronomy & Astrophysics*, 538, A26
- Roming, P. W., Kennedy, T. E., Mason, K. O., et al. 2005, *Space Science Reviews*, 120, 95
- Sahakyan, N., Giommi, P., Padovani, P., et al. 2023, *Monthly Notices of the Royal Astronomical Society*, 519, 1396
- Saldana-Lopez, A., Domínguez, A., Pérez-González, P. G., et al. 2021, *Monthly Notices of the Royal Astronomical Society*, 507, 5144
- Salvato, M., Hasinger, G., Ilbert, O., et al. 2008, *The Astrophysical Journal*, 690, 1250
- Salvato, M., Ilbert, O., Hasinger, G., et al. 2011, *The Astrophysical Journal*, 742, 61
- Sheng, Y., Rajagopal, M., Kaur, A., et al. 2024, *The Astrophysical Journal*, 964, 63
- Silver, R., Marchesi, S., Marcotulli, L., et al. 2020, *The Astrophysical Journal*, 902, 23
- Smith, J. A., Allam, S. S., Tucker, D. L., et al. 2006

Stroh, M. C., & Falcone, A. D. 2013, *The Astrophysical Journal Supplement Series*, 207, 28

Tagliaferri, G., Antonelli, L., Chincarini, G., et al. 2005, *Astronomy & Astrophysics*, 443, L1

Truebenbach, A. E., & Darling, J. 2017, *ApJS*, 233, 3

Urry, C. 1993, arXiv preprint astro-ph/9304003

Urry, C. M., & Padovani, P. 1995, *Publications of the Astronomical Society of the Pacific*, 107, 803